Received: 18 July 2025 | Accepted: 23 October 2025

DOI: 10.1111/2041-210x.70196

Methods in Ecology and Evolution

APPLICATION

theRmalUAV: An R package to clean and correct thermal UAV data for accurate land surface temperatures

Christophe Metsu[1,2] | Wouter H. Maes[3] | Sam Ottoy[1,4,5] | Koenraad Van Meerbeek[1,2]

[1]Division Forest, Nature and Landscape, Department Earth and Environmental Sciences, KU Leuven, Leuven, Belgium

[2]KU Leuven Plant Institute, KU Leuven, Leuven, Belgium

[3]Department of Plants and Crops, UAV Research Centre, Ghent University, Ghent, Belgium

[4]Bio-Research, PXL University College, Diepenbeek, Belgium

[5]Center for Environmental Sciences, Hasselt University, Diepenbeek, Belgium

Correspondence
Christophe Metsu
Email: christophe.metsu@kuleuven.be

Funding information
KU Leuven, Grant/Award Number: C14/22/067

Handling Editor: Sarah Goslee

Abstract

1. Thermal cameras on unoccupied aerial vehicles (UAVs) are increasingly being used in environmental and ecological research, including hydrology, wildfire detection and prediction, urban heat studies, precision agriculture, ecosystem functioning, wildlife monitoring and microclimate studies.
2. Converting raw thermal signals to quantitative land surface temperature (LST) values requires careful application of correction procedures. However, these steps are often overlooked or ignored—either due to limited expertise in thermal remote sensing or because of the technical complexity involved. Neglecting corrections for atmospheric effects and surface emissivity can lead to discrepancies of up to 5°C in the resulting LST estimate.
3. We introduce theRmalUAV, an R package that facilitates LST processing with two workflows: an orthomosaic-based and an image-based approach. The orthomosaic workflow applies a single function to the entire dataset, whereas the image-based workflow can account for variations in environmental conditions during the flight that affect surface temperature. The package corrects for atmospheric effects, background temperature, spatial emissivity and weather fluctuations, incorporating a novel method to handle rapid illumination changes. The package currently supports 11 common thermal sensors. It also includes tools for data cleaning, co-registration and reporting.
4. We demonstrate both the importance of the workflow and its implementation using two distinct case studies to highlight its versatility. The main text presents a detailed example using the research-grade TeAx ThermalCapture 2.0. A complementary example, featuring the more commercially oriented DJI Mavic 3T, is provided in the Supporting Information. For comprehensive guidance and tutorials, readers are directed to the package vignette and its companion website.

KEYWORDS
drones, land surface temperature, R package, remote sensing, thermal infrared, TIR, UAS, UAV

1 | INTRODUCTION

Surface temperature is a critical variable across various domains, from industrial applications to environmental studies. It serves as a key parameter in describing the energy balance between a surface and its surroundings, through its direct relationship with emitted long-wave infrared radiation (LWIR, 8–14 μm). This energy balance, or derived thermal metrics, can provide deeper insights into the properties and processes occurring within the object. Its potential is being explored across diverse research fields, including evaporation estimation (Hoffmann et al., 2016), wildfire detection and prediction (Allison et al., 2016), urban heat island studies (Henn & Peduzzi, 2024) and ecological research at different scales (Farella et al., 2022). In many of such applications, the retrieval of the correct and unbiased temperature is essential. This is for instance the case in stress detection of vegetation in precision agriculture (Messina & Modica, 2020), measuring thermal niches and detecting warm and cold spots to identify microrefugia in topographically complex areas such as mountains (Hoffrén & García, 2023), measuring thermally suitable areas for vegetation restoration (Ruan et al., 2022) and assessing thermal heterogeneity within ecosystems or the broader functioning of entire ecosystems, such as grasslands (Lyu et al., 2022).

Advancements in remote sensing technologies led to cost reductions and the miniaturization of sensors, promoting the use of unoccupied aerial vehicles (UAVs or drones) in ecological and environmental research (Manfreda et al., 2018). Compared to traditional handheld thermal cameras or thermal satellite imagery, UAVs provide high spatial resolution and flexibility, enabling the acquisition of spatially continuous datasets with very high resolution. The integration of thermal infrared cameras on UAV platforms allows for measuring the incoming LWIR and the direct derivation of land surface temperatures (LST).

The direct temperature estimate from the sensor can deviate from the actual surface temperature. In general, there are two sources of error. The first source relates to the sensor accuracy and the way the measurements were obtained. These relate to sensor calibration, sensor stabilization before the flight, flight speed and wind speed deviation during the flight; see Kelly et al. (2019) and Maes (2025) to avoid or minimize these errors. The second source relates to atmospheric correction and conversion of brightness to surface temperature; these errors are explained in more detail in the Supporting Information: Appendix 1. Consequently, thermal infrared data acquired from UAVs often require essential corrections.

The complexity of the necessary corrections and the potential limited expertise in thermal remote sensing among environmental scientists and other UAV researchers, often results in incomplete or incorrect application of these corrections. Therefore, we developed the user-friendly R package theRmalUAV for cleaning and correcting thermal UAV data. This package aims to facilitate the implementation of fundamental corrections necessary to obtain optimal results from UAV thermal imagery. The methods and workflow are based on known physical formulae and the recommendations of Maes et al. (2017) and Heinemann et al. (2020), with additional new functionalities. To help users understand the features in this package, we strongly advise the reader to go through the thermal remote sensing background provided in the Supporting Information: Appendix 1. In the next section, we will go over the implementation and explain the basic functionalities, followed by an elaborate example in Section 3.

2 | IMPLEMENTATION OF theRmalUAV

The R package can be installed from (https://github.com/christophemetsu/theRmalUAV). It offers two main workflows and an optional extension (Figure 1):

1. *Image-based workflow*: Applies atmospheric and background temperature corrections to individual raw thermal images prior to orthomosaic generation using external photogrammetry software. This allows for adjustment of changing environmental conditions during the flight that affect the surface temperature (e.g. air temperature). We recommend this workflow as the preferred best practice for processing UAV-based thermal imagery.
2. *Orthomosaic-based workflow*: Applies corrections directly to a brightness temperature orthomosaic. This is suitable when processing individual raw images is complicated or risk altering metadata. It is ideal for multispectral cameras with a low-resolution thermal band relying on higher-resolution bands for aligning and mosaicking in photogrammetry software (e.g. Micasence Altum-PT).
3. *Spatial emissivity correction* (*optional extension*): If the land cover is heterogeneous, emissivity values can differ. In this case, the spatially explicit emissivity correction is recommended. This uses either an NDVI or a landcover map. This is integrated in *ortho_correct()* for the orthomosaic workflow and conducted post hoc using *tuav_emis()* in the image-based approach.

Additional functionalities are discussed in Section 2.2.5, further documentation is available in the vignettes of the R package and its website (https://christophemetsu.github.io/theRmalUAV/).

2.1 | Data collection

The initial step involves collecting the thermal images. Camera compatibility can be checked using *tuav_cameras()*, which lists supported cameras, including: TeAx ThermalCapture(2.0), Micasense Altum(-PT), DJI Mavic 3T/4T, Matrice 3TD/30T (both normal and super-resolution mode) and Zenmuse H20N/H20T/H30T. DJI cameras store thermal images as JPG and require specific preprocessing before conversion to temperature data. Therefore, the DJI Thermal Infrared Processing (DIRP) libraries (only available for Windows and Linux) are embedded in the package (see Supporting Information: Appendix 2 for more information).

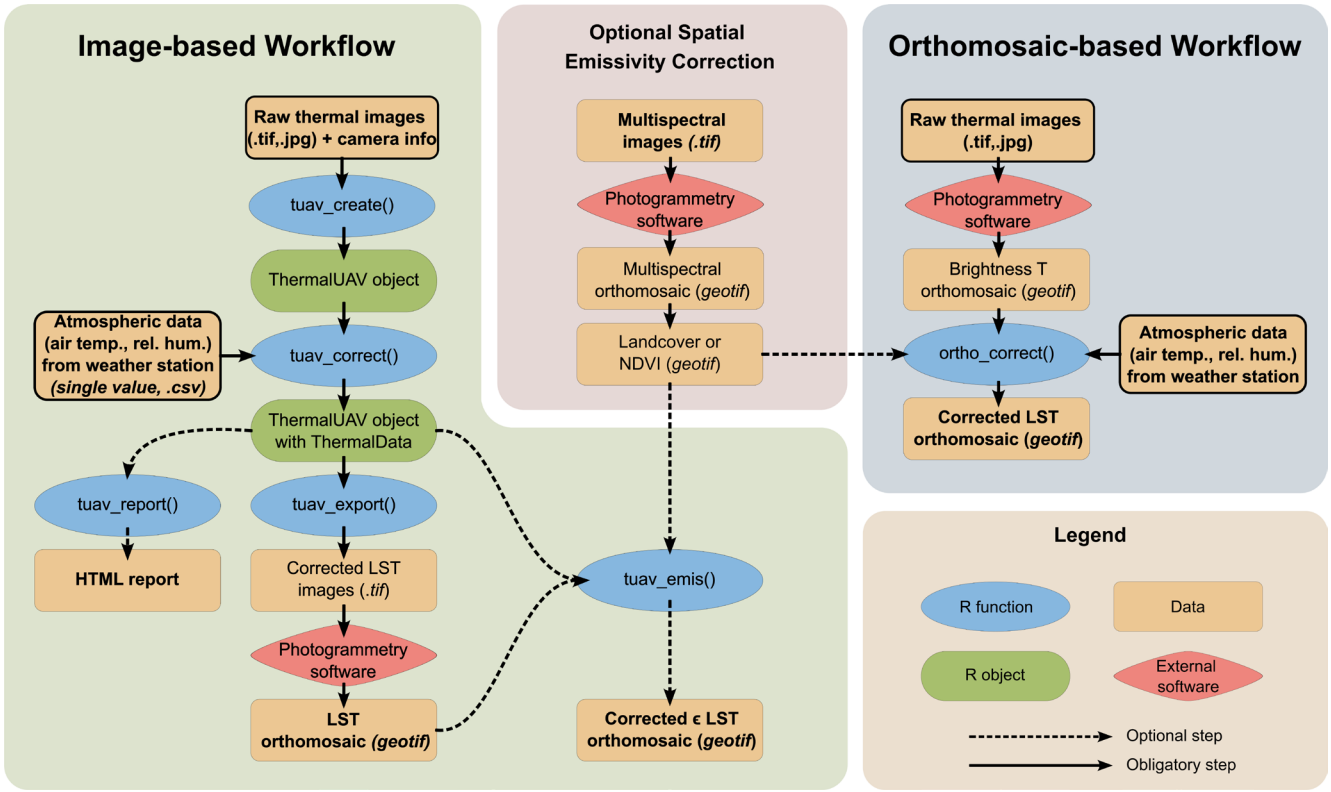

FIGURE 1 Overview of the theRmalUAV workflows. The image-based workflow (green box) converts raw thermal images to corrected LST images, while the othomosaic-based workflow (blue box) converts a brightness temperature orthomosaic into a corrected LST orthomosaic. The optional spatial emissivity correction (pink box) can be applied in both workflows. Initial data and final outputs are indicated in bold with their data format; required inputs are outlined in black. Atmospheric data (air temperature and relative humidity) are retrieved from a portable weather station or a meteorological weather station/website.

UAV flight guidelines and best practices are provided in Maes (2025). To capture atmospheric variability, we recommend recording air temperature (°C) and relative humidity (%) at high frequency (e.g. in 5-s intervals) using a portable weather station (Kelly et al., 2019). Alternatively, data from the nearest meteorological station may be used. Accurate background temperature (T_{bg}) measurement—detailed in the Supporting Information: Appendix 1—can be achieved by imaging a reference panel covered with crumpled aluminium foil using the thermal camera. Due to its low emissivity, the aluminium panel reflects nearly all incoming thermal radiation, providing an effective estimate of the background temperature. The panel should be large enough to cover at least nine pixels in the thermal image, minimizing mixed-pixel effects.

2.2 | The image-based workflow

2.2.1 | Create ThermalUAV object

The image-based workflow uses a custom R object of class ThermalUAV, which organizes key variables in slots using structured lists: *Info*, *Position*, *Sharpness*, *Atmosphere*, *Smooth* and *ThermalData*. These components are progressively filled and used, enabling a streamlined and flexible processing pipeline. The ThermalUAV object is initialized with *tuav_create()*.

2.2.2 | Conversion of at-sensor temperature to LST

The function *tuav_correct()* applies image-level corrections to a ThermalUAV object using atmospheric data (retrieved from a portable weather station or the closest meteorological station), supplied as:

(i) single values of air temperature (T_{air}, °C) and relative humidity (ω%),
(ii) vectors of T_{air} and ω% matching the image count,
(iii) a time-stamped data frame covering at least the flight duration or
(iv) T_{air} can be estimated via a trimmed mean of thermal pixel values, when air temperature was not measured.

Water vapour content and subsequently transmittance (τ) are computed for each image, followed by LST estimation with a user-defined emissivity value (ϵ) (Heinemann et al., 2020):

$$\mathrm{LST} = \sqrt[4]{\frac{T_{\mathrm{sens}}^4 - (1-\epsilon)\ \tau\ T_{\mathrm{bg}}^4 - (1-\tau)\,T_{\mathrm{air}}^4}{\epsilon\ \tau}} \quad (1)$$

with T_{sens} the at-sensor temperature (K), T_{bg} the background temperature (K) and T_{air} the free-air temperature (°C). If T_{bg} is not measured, it can be estimated based on T_{air} and specified sky conditions (clear or overcast). The used formulae, steps and additional information are outlined in the Supporting Information: Appendix 1. The function reads the thermal TIFF files with the at-sensor temperatures and stores LST outputs as matrices under the ThermalData slot, returning an updated ThermalUAV object. If emissivity is set to 1, background temperature and emissivity corrections are not taken into account (Equation 1), and brightness temperature is returned—useful for later spatial emissivity correction (Section 2.2.4). Note that *tuav_correct()* does not account for the influence of T_{air} on LST (Maes et al., 2017); this can be addressed post hoc using *tuav_smooth()* (Section 2.2.5).

2.2.3 | Exporting and mosaicking

Following correction, the ThermalData can be exported using *tuav_export()*, writing each image as a 16-bit geotagged TIFF in centikelvin (labelled *original_filename_corrected.tif*) with two-decimal precision. Metadata—including GNSS position, altitude and camera orientation—is embedded for downstream processing. These corrected images can be imported into photogrammetry software (e.g. Agisoft Metashape, Pix4D Mapper) to generate an LST orthomosaic. Note that geotagged images are not necessarily georeferenced and might not display correctly when imported directly into GIS software. To convert centikelvin values to degrees Celsius, divide by 100 and subtract 273.15. An optional HTML report can be generated with *tuav_report()*, summarizing correction parameters, displaying camera positions on an interactive map and providing mission details.

2.2.4 | Emissivity correction

In heterogeneous landscapes, spatially explicit emissivity correction is recommended. The function *tuav_correct()* applies only a single emissivity value, since image-level spatially explicit emissivity correction is inaccurate due to uncertainties in image alignment and viewing angles. The post-processing function *tuav_emis()* allows for emissivity correction on georeferenced LST orthomosaics. This function back-transforms pixel values to at-sensor temperature using the original parameters from the corresponding ThermalUAV object. LST is then recalculated per pixel using spatially explicit emissivity via one of three methods (Heinemann et al., 2020; Li et al., 2013): (i) the NDVI threshold method estimating emissivity from vegetation cover fraction (see Supporting Information: Appendices 1 and 3), requiring an NDVI map along with threshold values of NDVI and emissivity for soil and vegetation (Valor & Caselles, 1996); (ii) a land cover map paired with a two-column matrix of classes and emissivity values from databases like Salisbury and D'Aria (1992); or (iii) a direct emissivity map. The maps may be obtained from different sources or platforms, provided they are spatially aligned, are of sufficient resolution for the desired detail and are representative for the scene.

2.2.5 | Other functionalities

Besides the core functions (Figure 1), the *theRmalUAV* package includes supplementary tools. Table 1 briefly outlines some functions; other functionalities and detailed information are available in the package's reference and vignettes. All functions operate on a ThermalUAV object and return an updated one, unless specified otherwise.

2.3 | The orthomosaic-based workflow

The orthomosaic-based workflow applies corrections directly to brightness temperature orthomosaics using Equation (1). This requires prior stitching of raw thermal images in photogrammetry software. Depending on the camera, conversion to Kelvin may be necessary when data are provided in centikelvin or as digital numbers, requiring a linear transformation. The *ortho_correct()* function assumes constant atmospheric conditions—single values for air temperature (T_{air}) and relative humidity (ω%)—limiting the ability to account for changing environmental conditions, such as the effect of T_{air} on LST (Maes et al., 2017). For short flights under stable weather, this assumption is unlikely to substantially affect results. Emissivity can be specified as a single value for the entire map or corrected spatially, recommended practice, using one of three methods as outlined in Section 2.2.4.

3 | EXAMPLE OF THE IMAGE-BASED WORKFLOW

3.1 | Data collection

We demonstrate the image-based workflow using data from a heterogeneous patch within the Kalmthoutse Heide (Figure 2a), a heathland ecosystem in Belgium (permission granted by ANB [Agentschap Natuur en Bos]). The site comprises *Calluna vulgaris* shrubs on sandy soils, interspersed with mosses, bare ground, scattered *Pinus sylvestris* and shallow ponds (Figure 2b). A UAV flight was conducted on July 19, 2024, at 14:00 local time under clear sky conditions, using a DJI Matrice 300 RTK equipped with (i) the multispectral Micasense Altum-PT and (ii) a TeAx ThermalCapture 2.0 with ThermalCapture Calibrator. The flight followed a single-grid pattern at 75 m above ground level with 80% side overlap and a speed of 4.5 m/s, yielding a ground sampling distance (GSD) of 3.28 cm (multispectral)

TABLE 1 Additional functions available within the image-based workflow.

	Function	Description
Position functions	*tuav_loc()*	Computes camera locations/image extents as a *terra::SpatVector* object. Optionally calculates mean frontal image overlap
	tuav_view()	Visualizes camera locations/image extents on an interactive map for visual inspection and data cleaning
	tuav_coreg()	Optimizes thermal camera positions and viewing angles using co-registered high-resolution cameras with precise GNSS data. Done either directly or via optimized camera positions derived after alignment of the high-resolution camera in Agisoft Metashape. If using the latter, *coreg_prep()* prepares the required input format. The optimized parameters are saved in the updated ThermalUAV object and used during export
Cleaning	*tuav_persec()*	Reduces data volume by retaining a specified number of The sharpest images per second. Useful for high-frequency thermal image acquisition
	tuav_reduc()	Filters images based on either minimum frontal overlap or sharpness threshold, helping to reduce data volume from high-frequency thermal recordings
Correcting	*tuav_smooth()*	Applies temporal smoothing to LST images in ThermalData (post-*tuav_correct()*). Two methods are available: • "T_air": Adjusts for air temperature effects on LST, following Maes et al. (2017) • "image": Mitigates abrupt temperature fluctuations (e.g., from cloud cover or wind gusts) based on image-derived values. See Supporting Information: Appendix 3 for algorithm details and an elaborate example

Note: Unless specified otherwise, all functions can be applied to ThermalUAV objects at any stage of the processing.

and 9.66 cm (thermal). Air temperature and relative humidity were recorded every 5 s using a Kestrel 5500 L environmental meter mounted 1.5 m above ground. Mean values during the flight were 28.3°C and 42.7%, respectively.

3.2 | Pre-processing

Multispectral data were processed in Agisoft Metashape Professional 2.0.0 following the standard workflow (Agisoft Metashape, 2024). Reflectance calibration was based on images of a 60×60 cm calibration panel with 50% reflectance, captured at flight altitude. As the thermal camera was co-registered with the Micasense Altum-PT, we demonstrate the optional co-registration workflow. Consequently, the camera references were exported as a CSV file, including the rotation and estimated values to 7 decimal places. Thermal imagery, initially stored in TMC format, was converted to TIFF using ThermoViewer 3.0.10 (TeAx), with associated metadata exported as a single CSV file.

3.3 | Processing using the theRmalUAV package

We first create a ThermalUAV object collecting all the necessary metadata using *tuav_create()*:

```
library(theRmalUAV)
thermaluav <- tuav_create(path = "Data/TIFs/",
                          camera = "ThermalCapture",
                          meta_csv = "Data/TIFs/
                          Example_meta.csv",
                          flight_height=75)
```

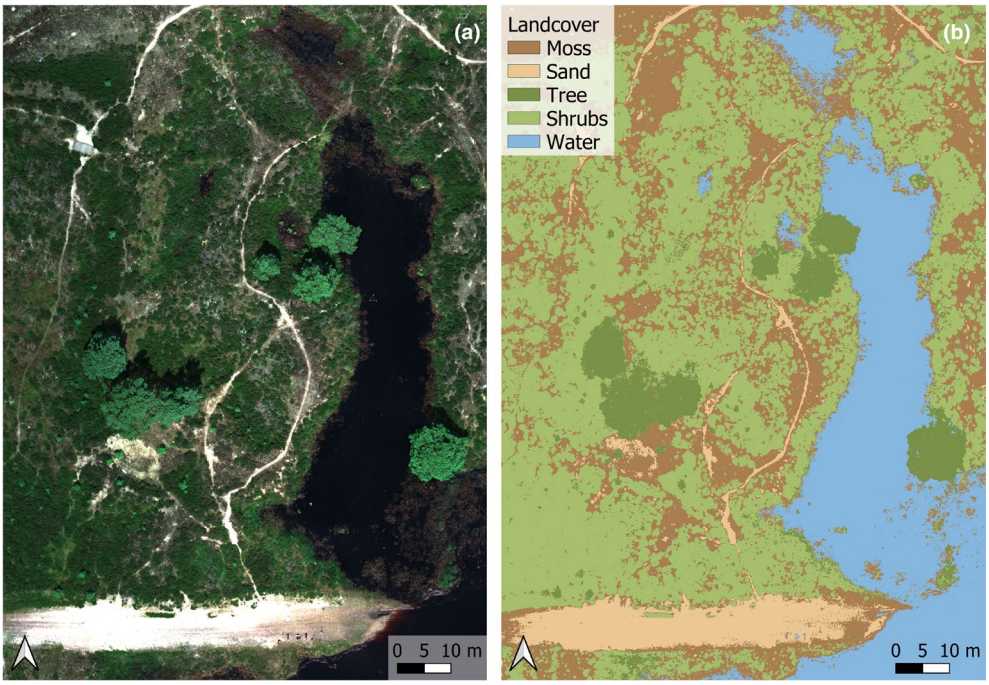

FIGURE 2 (a) RGB composite from the Micasense Altum-PT. (b) Land cover map showing the diverse landscape consisting of moss, sand, trees, shrubs and water.

Here, we used the metadata file exported from ThermoViewer, for most cameras, this option is omitted and the metadata is read from the EXIF data. Our camera recorded 1237 images at 8.33 Hz. Using *tuav_reduc()* with a minimum frontal overlap of 85%, the dataset was reduced to 125 sharp images. The resulting ThermalUAV object was saved as a new variable to avoid overwriting the previous ThermalUAV object:

```
thermaluav_reduc <-  tuav_reduc(thermaluav,
                                method = "Overlap",
                                min_overlap=0.85)
```

Image-level corrections were performed using *tuav_correct()*, with the air temperature (T_air) and relative humidity (rel_hum) from the time-stamped Kestrel dataset. Emissivity was set to 1 to retrieve brightness temperature, allowing for spatial emissivity correction later on:

```
thermaluav_correct <- tuav_correct(thermaluav_reduc,
                                   flight_height=75,
                                   T_air = Kestrel,
                                   rel_hum = Kestrel,
                                   T_bg=274.2,
                                   emiss=1)
```

To adjust for the effect of varying air temperature on LST, *tuav_smooth()* was applied using method "T_air":

```
thermaluav_smooth <- tuav_smooth(thermaluav_correct,
                                 method = "T_air")
```

The ThermalCapture 2.0 was rigidly mounted to a Micasense Altum-PT, which provides high-accuracy RTK GNSS data. To benefit from this co-registration, we used optimized camera positions from the Altum-PT, exported from Agisoft Metashape. First, the Metashape-derived camera references were reformatted using *coreg_prep()*; then, thermal image positions and viewing angles were optimized via *tuav_coreg()*. The rig offset values, relative to the Altum-PT green band (band 2), are in millimetres. Details on the rig offset values are in Supporting Information: Appendix 4:

```
sfm_cameras <- coreg_prep(img_path = "Data/
                          Micasense/000/",
                          SfM_option = "Agisoft
                          Metashape",
                          opt_camera_path = "Data/
                          Micasense/Reference
                          Cameras_example.txt",
                          camera_name = "Altum-PT_
                          MSP",
                          label = "_2",
                          timezone = "UTC")
thermaluav_coreg <- tuav_coreg(thermaluav_smooth,
                               opt_cameras = sfm_
                               cameras,
                               rig_offset = c(46,
                               -103, 20, 0, 0, 0))
```

The final ThermalUAV object, now containing brightness temperature data (as we used an emissivity of 1) and optimized geolocation information, was exported as geotagged TIFF files using

tuav_export(). These files store temperatures in centikelvin with two-decimal precision in a 16-bit format:

```
tuav_export(thermaluav_coreg)
```

The TIFF files were processed in Agisoft Metashape using standard multispectral workflow parameters (Agisoft Metashape, 2024) to generate a thermal orthomosaic, then converted to degrees Celsius and exported as a GeoTIFF. To retrieve LST, spatial emissivity correction was applied using the land cover method in *tuav_emis()*, with a matrix linking land cover classes to emissivity values (Table 2; Rubio et al., 1997).

TABLE 2 Land cover classes with their corresponding emissivity values.

Label	Land cover	Emissivity
1	Dry mosses	0.962
2	Sand	0.914
3	Tree	0.983
4	Shrubs	0.984
5	Water	0.991

The function also requires the original temperature GeoTIFF—here the brightness temperature built in Agisoft Metashape—a map to base our corrections on—here the land cover map—and the last ThermalUAV object related to this project to retrieve atmospheric parameters and T_{bg}.

```
matrix <- matrix(c(1,2,3,4,5,0.962,0.914,0.983,
0.984,0.991), ncol=2)
thermaluav_emis <- tuav_emis(thermal_orig ="Data/
                             Example_Tbright.tif",
                             thermal_uav =
                             thermaluav_coreg,
                             temp = "C",
                             corrmap = "Data/
                             Example_LC.tif",
                             method = "LC",
                             write_Ts = TRUE,
                             filename_Ts =
                             "Example_Tsurf.tif",
                             LC_emiss_matrix =
                             matrix)
```

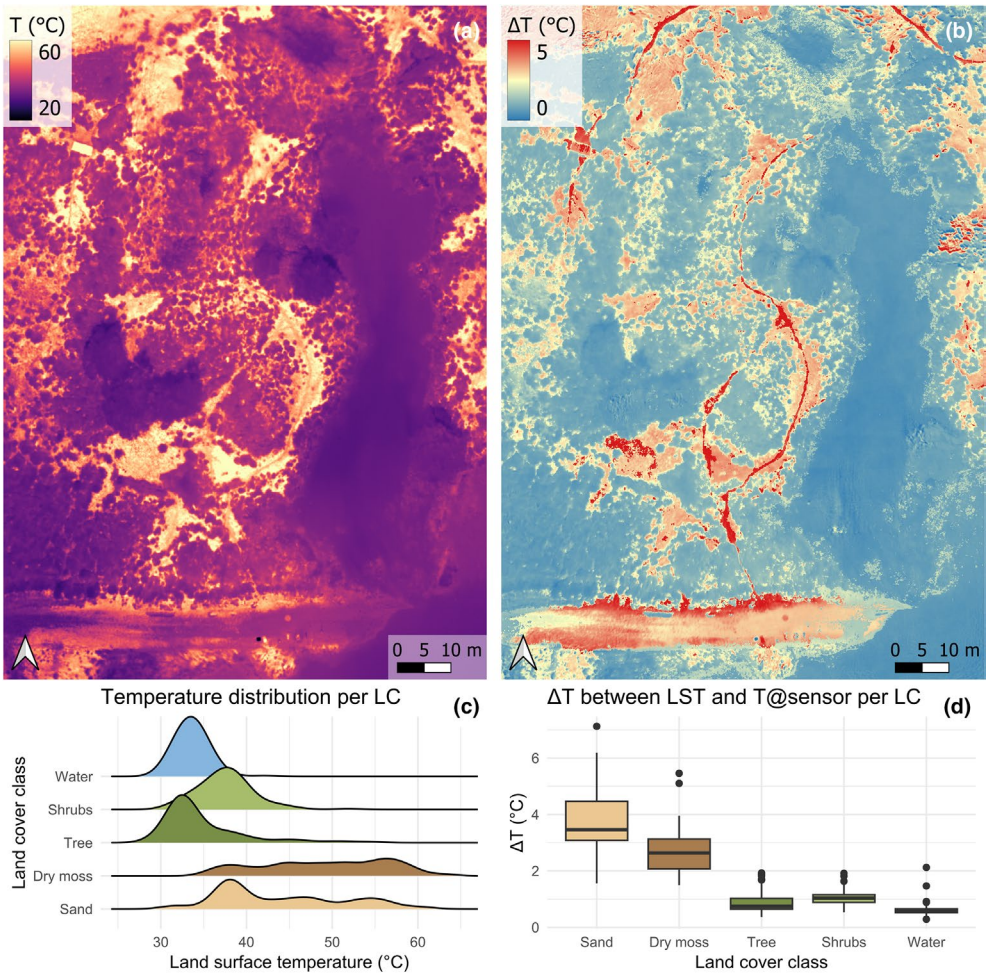

FIGURE 3 (a) Final LST map of the area representing the temperatures in°C. (b) Temperature difference (Δ*T*) between the LST and the at-sensor temperature. (c) Temperature distribution per land cover class from a stratified random sample of 100 pixels per class. (d) Δ*T* between the LST and at-sensor temperature per LC [same sample as in (c)].

3.4 | Results

The final LST map illustrates the wide range of temperatures in this heterogeneous landscape on a hot, sunny day (Figure 3a,c). Bare sandy areas reach temperatures up to 50°C, while dark, dry mosses exhibit extreme surface temperatures up to 60°C due to the absorption of shortwave solar radiation and a lack of evapotranspiration. According to the LST map, the shallow, still pond reached a surface temperature of approximately 31°C.

The at-sensor temperature substantially underestimates the LST, with temperature differences reaching up to 5°C (Figure 3b,d). The largest discrepancies are observed in areas with extreme temperatures and/or land covers with low emissivity values (e.g. bare sand, Figures 2b and 3d). The waterbody and trees, with lower temperatures and emissivity values nearing 1, show smaller discrepancies (around 0.5°C, Figure 3c,d).

To further illustrate the correction's effect for this example, the differences between a range of at-sensor temperatures and the final LST per land cover class (and thus, emissivity), including the brightness temperature, are plotted in Figure 4. These differences were calculated using Equation (1) using the mean atmospheric conditions during the flight: $\tau = 0.9368$, $T_{air} = 28.26$°C and $T_{bg} = 274.2$ K. The emissivity values for each class are shown in Table 2, and to obtain the brightness temperature, the emissivity was set to 1. The atmospheric correction's influence is minimal when the at-sensor temperature approximates the free-air temperature, but becomes significant at very high temperatures (up to 2°C in this example). When accounting for emissivity and background temperature, the discrepancies become more prominent, especially at extreme temperatures and where the surface substantially deviates from the black body behaviour. This trend aligns with Figure 3b, where the largest discrepancies occur on the bare soil (low emissivity) and at the patches of dry moss (extreme temperatures).

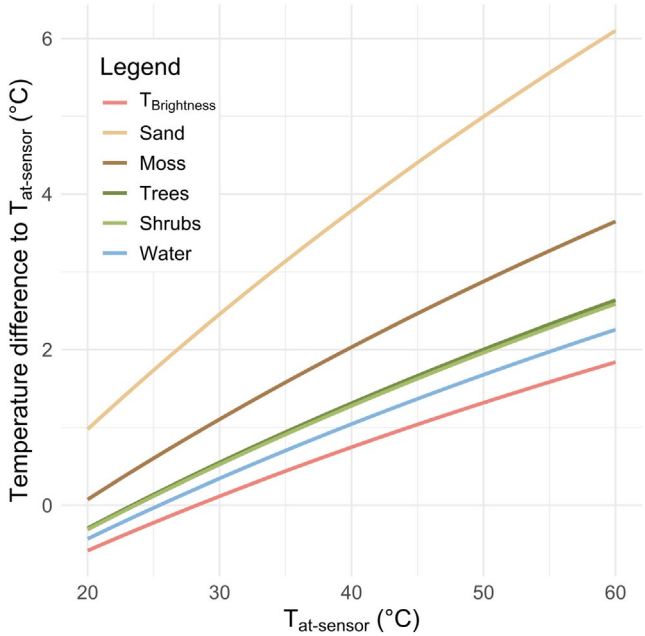

FIGURE 4 Temperature differences relative to at-sensor temperature under sunny conditions. Brightness temperature ($\epsilon = 1$, red) exceeds at-sensor temperature when the latter is higher than the air temperature. Differences to final LST are shown per land cover class, based on class-specific emissivity values ($\epsilon_{sand} = 0.914$, $\epsilon_{moss} = 0.962$, $\epsilon_{tree} = 0.983$, $\epsilon_{shrub} = 0.984$, $\epsilon_{water} = 0.991$). Values were computed using Equation (1) with mean flight conditions: Transmittance = 0.9368, air temperature = 28.26°C, background temperature = 274.2 K.

4 | CONCLUSION

The theRmalUAV R package integrates state-of-the-art correction methods into a flexible, user-friendly and open-source framework for deriving land surface temperature (LST) from UAV-based thermal imagery. By streamlining complex processing steps—including atmospheric and emissivity corrections—it addresses a critical gap in accessibility for environmental scientists with limited expertise in thermal remote sensing.

The package provides two complementary workflows: an image-based workflow with fine-grained control over individual image corrections and an orthomosaic-based workflow offering an alternative for pre-stitched thermal mosaics. Advanced features in the image-based workflow include corrections for intra-flight atmospheric variability, the influence of air temperature on surface temperature and a novel approach for smoothing rapid temperature fluctuations using image-derived data.

Additional tools support data cleaning, camera co-registration and automated reporting. Spatially explicit emissivity correction—via NDVI or land cover classification—is implemented in both workflows. Together, these functionalities enable complete processing of thermal UAV data while preserving essential metadata for downstream photogrammetry. The package is demonstrated through applied use cases, with further guidance available in the accompanying documentation and vignettes.

AUTHOR CONTRIBUTIONS

Christophe Metsu and Wouter H. Maes conceived the ideas and designed methodology; Christophe Metsu, Sam Ottoy and Wouter H. Maes collected the data; Christophe Metsu analysed the data; Christophe Metsu led the writing of the manuscript. All authors contributed critically to the drafts and gave final approval for publication.

ACKNOWLEDGEMENTS

The author thanks Wouter H. Maes for his valuable insights into thermal UAV remote sensing and the initial development of the script, Koenraad Van Meerbeek for constructive feedback on the storyline and Sam Ottoy for support during the UAV field campaigns. This study was funded by the Internal Funds of KU Leuven (MICROMICS project; C14/22/067), with support from the University Foundation of Belgium (Universitaire Stichting van België) to sGlobe lab (KU Leuven). The author is also grateful to the reviewers for their helpful comments that improved the clarity and interpretability of the manuscript and to Jef De Winter from ANB (Agentschap Natuur en Bos, Belgium) for permission to conduct research in the beautiful Grenspark Kalmthoutse Heide. During the preparation of this work, the lead author used

Microsoft Copilot and GPT-4 in order to improve the readability and language of the manuscript. After using this tool, the author reviewed and edited the content as needed and takes full responsibility for the content of the published article.

CONFLICT OF INTEREST STATEMENT

The authors declare no conflicts of interest.

PEER REVIEW

The peer review history for this article is available at https://www.webofscience.com/api/gateway/wos/peer-review/10.1111/2041-210x.70196.

DATA AVAILABILITY STATEMENT

The R package code is open-source and available on GitHub at https://github.com/christophemetsu/theRmalUAV. The version of the package used in this manuscript is available via https://doi.org/10.5281/zenodo.17475728 (Metsu, 2025a). Data is available via https://doi.org/10.6084/m9.figshare.28648817 (Metsu, 2025b).

ORCID

Christophe Metsu https://orcid.org/0000-0002-5153-9351
Wouter H. Maes https://orcid.org/0000-0002-1592-9299
Sam Ottoy https://orcid.org/0000-0002-1216-9570
Koenraad Van Meerbeek https://orcid.org/0000-0002-9260-3815

REFERENCES

Agisoft Metashape. (2024). *MicaSense Altum processing workflow (including Reflectance Calibration) in Agisoft Metashape Professional*. https://agisoft.freshdesk.com/support/solutions/articles/31000148381-micasense-altum-processing-workflow-including-reflectance-calibration-in-agisoft-metashape-professi

Allison, R. S., Johnston, J. M., Craig, G., & Jennings, S. (2016). Airborne optical and thermal remote sensing for wildfire detection and monitoring. *Sensors (Basel)*, *16*(8), 1310. https://doi.org/10.3390/s16081310

Farella, M. M., Fisher, J. B., Jiao, W., Key, K. B., & Barnes, M. L. (2022). Thermal remote sensing for plant ecology from leaf to globe. *Journal of Ecology*, *110*(9), 1996–2014. https://doi.org/10.1111/1365-2745.13957

Heinemann, S., Siegmann, B., Thonfeld, F., Muro, J., Jedmowski, C., Kemna, A., Kraska, T., Muller, O., Schultz, J., Udelhoven, T., Wilke, N., & Rascher, U. (2020). Land surface temperature retrieval for agricultural areas using a novel UAV platform equipped with a thermal infrared and multispectral sensor. *Remote Sensing*, *12*(7), 1075. https://doi.org/10.3390/rs12071075

Henn, K. A., & Peduzzi, A. (2024). Surface heat monitoring with high-resolution UAV thermal imaging: Assessing accuracy and applications in urban environments. *Remote Sensing*, *16*(5), 930. https://doi.org/10.3390/rs16050930

Hoffmann, H., Nieto, H., Jensen, R., Guzinski, R., Zarco-Tejada, P., & Friborg, T. (2016). Estimating evaporation with thermal UAV data and two-source energy balance models. *Hydrology and Earth System Sciences*, *20*(2), 697–713. https://doi.org/10.5194/hess-20-697-2016

Hoffrén, R., & García, M. B. (2023). Thermal unmanned aerial vehicles for the identification of microclimatic refugia in topographically complex areas. *Remote Sensing of Environment*, *286*(June 2022), 113427. https://doi.org/10.1016/j.rse.2022.113427

Kelly, J., Kljun, N., Olsson, P.-O., Mihai, L., Liljeblad, B., Weslien, P., Klemedtsson, L., & Eklundh, L. (2019). Challenges and best practices for deriving temperature data from an Uncalibrated UAV thermal infrared camera. *Remote Sensing*, *11*(5), 567. https://doi.org/10.3390/rs11050567

Li, Z. L., Wu, H., Wang, N., Qiu, S., Sobrino, J. A., Wan, Z., Tang, B. H., & Yan, G. (2013). Land surface emissivity retrieval from satellite data. *International Journal of Remote Sensing*, *34*(9–10), 3084–3127. https://doi.org/10.1080/01431161.2012.716540

Lyu, X., Li, X., Dang, D., Dou, H., Wang, K., & Lou, A. (2022). Unmanned aerial vehicle (UAV) remote sensing in grassland ecosystem monitoring: A systematic review. *Remote Sensing*, *14*(5), 1–19. https://doi.org/10.3390/rs14051096

Maes, W. H. (2025). Practical guidelines for performing UAV mapping flights with snapshot sensors. *Remote Sensing*, *17*(4), 606. https://doi.org/10.3390/rs17040606

Maes, W. H., Huete, A. R., & Steppe, K. (2017). Optimizing the processing of UAV-based thermal imagery. *Remote Sensing*, *9*(5), 476. https://doi.org/10.3390/rs9050476

Manfreda, S., McCabe, M. F., Miller, P. E., Lucas, R., Madrigal, V. P., Mallinis, G., Dor, E. B., Helman, D., Estes, L., Ciraolo, G., Müllerová, J., Tauro, F., de Lima, M. I., Lima, J. L. M. P., Maltese, A., Frances, F., Caylor, K., Kohv, M., Perks, M., … Toth, B. (2018). On the use of unmanned aerial systems for environmental monitoring. *Remote Sensing*, *10*(4), 641. https://doi.org/10.3390/rs10040641

Messina, G., & Modica, G. (2020). Applications of UAV thermal imagery in precision agriculture: State of the art and future research outlook. *Remote Sensing*, *12*(9), 1491. https://doi.org/10.3390/RS12091491

Metsu, C. (2025a). *christophemetsu/theRmalUAV: theRmalUAV v1.1.1 (v1.1.1)*. Zenodo. https://doi.org/10.5281/zenodo.17475729

Metsu, C. (2025b). *theRmalUAV data (version 1)*. Figshare. https://doi.org/10.6084/m9.figshare.28648817.v1

Ruan, M., Hu, Z., Duan, X., Zhou, T., & Nie, X. (2022). Using UAV and field measurement technology to monitor the impact of coal gangue pile temperature on vegetation ecological construction. *Remote Sensing*, *14*(2), 353. https://doi.org/10.3390/rs14020353

Rubio, E., Caselles, V., & Badenas, C. (1997). Emissivity measurements of several soils and vegetation types in the 8–14, μm Wave band: Analysis of two field methods. *Remote Sensing of Environment*, *59*(3), 490–521. https://doi.org/10.1016/s0034-4257(96)00123-x

Salisbury, J. W., & D'Aria, D. M. (1992). Emissivity of terrestrial materials in the 8–14 μm atmospheric window. *Remote Sensing of Environment*, *42*(2), 83–106. https://doi.org/10.1016/0034-4257(92)90092-X

Valor, E., & Caselles, V. (1996). Mapping land surface emissivity from NDVI: Application to European, African, and South American areas. *Remote Sensing of Environment*, *57*(3), 167–184. https://doi.org/10.1016/0034-4257(96)00039-9

SUPPORTING INFORMATION

Additional supporting information can be found online in the Supporting Information section at the end of this article.

Appendix 1. Thermal remote sensing background.

Appendix 2. DJI cameras.

Appendix 3. Accounting for varying weather conditions.

Appendix 4. Calculation of rig offset values.

How to cite this article: Metsu, C., Maes, W. H., Ottoy, S., & Van Meerbeek, K. (2026). `theRmalUAV`: An R package to clean and correct thermal UAV data for accurate land surface temperatures. *Methods in Ecology and Evolution*, *17*, 488–496. https://doi.org/10.1111/2041-210x.70196